Exploring the Leidenfrost effect for the deposition of high-quality In₂O₃ layers via spray pyrolysis at low temperatures and their application in high electron mobility transistors

Ivan Isakov*, Hendrik Faber, Max Grell, Gwenhivir Wyatt-Moon, Nikos Pliatsikas, Thomas Kehagias, George P. Dimitrakopulos, Panos P. Patsalas, Ruipeng Li, and Thomas D. Anthopoulos*

Dr. I. Isakov, Dr. H. Faber, M. Grell, G. Wyatt-Moon, Prof. T. Anthopoulos
Blackett Laboratory and Centre for Plastic Electronics, Imperial College London, London, SW7 2AZ, United Kingdom
E-mails: i.isakov@imperial.ac.uk; thomas.anthopoulos@imperial.ac.uk

N. Pliatsikas, Prof. T. Kehagias, Prof. G. P. Dimitrakopulos, Prof. P. Patsalas
Department of Physics, Aristotle University of Thessaloniki, 54124 Thessaloniki, Greece

Dr. R. Li
Cornell High Energy Synchrotron Source, Wilson Laboratory Cornell University, Ithaca NY, 14853, USA

Prof. T. Anthopoulos
Materials Science and Engineering, Division of Physical Sciences and Engineering, King Abdullah University of Science and Technology, Thuwal 23955-6900, Saudi Arabia
E-mails: thomas.anthopoulos@kaust.edu.sa

Abstract

We study the growth mechanism of indium oxide (In₂O₃) layers processed via spray pyrolysis of an aqueous precursor solution in the temperature range of 100–300 °C and the impact on their electron transporting properties. Analysis of the droplet impingement sites on the substrate's surface as a function of its temperature reveals that Leidenfrost effect dominated boiling plays a crucial role in the growth of smooth, continuous and highly crystalline In₂O₃ layers via a vapour phase-like process. By careful optimization of the precursor formulation, deposition conditions and choice of substrate, we are able to exploit this effect and grow ultra-thin and exceptionally smooth layers of In₂O₃ over large area substrates at temperatures as low as 252 °C. Thin-film transistors (TFTs) fabricated using these optimised In₂O₃ layers exhibit

superior electron transport characteristics with the electron mobility reaching up to 40 cm^2 V^{-1} s^{-1}, a value amongst the highest reported to date for solution-processed In$_2$O$_3$ TFTs. The present work contributes enormously to the basic understanding of spray pyrolysis and highlights its tremendous potential for large-volume manufacturing of high-performance metal oxide thin-film transistor electronics.

1. Introduction

Solution processed metal oxide thin-film transistors (TFTs) are promising candidates for the use in ubiquitous flexible electronics due to their low cost, high charge carrier mobility and optical transparency.[1–3] A large volume of research in recent years has been dedicated in reducing the processing temperature of solution-processed metal oxide devices in an effort to improve their compatibility with flexible plastic substrates, such as polyethylene naphthalate and polyimide, without compromising their performance.[4] This goal is of paramount importance, since in order for these material systems to be able to compete with current TFT technologies (amorphous silicon (a-Si), sputtered indium-gallium-zinc-oxide etc.) the charge carrier mobility of solution processed metal oxide TFTs should exceed the benchmark value of 10 cm^2 V^{-1} s^{-1}.[4]

Indium oxide (In$_2$O$_3$) is an attractive metal oxide semiconductor for TFT applications because in its crystalline form the electron mobility can reach values as high as 220 cm^2 V^{-1} s^{-1}. [5–7] Numerous studies reported solution processing of In$_2$O$_3$, with resulting TFTs prepared below 300 °C now routinely reaching mobilities of 15–20 cm^2 V^{-1} s^{-1}.[8–10] The most commonly used methods of manufacturing In$_2$O$_3$ TFT from solution phase include spin-coating, spray-coating, blade-coating and inkjet printing. [11–14] While the bulk of the research has so far exploited spin coating, the method lacks potential for large area manufacturing, especially within the display industry. Spray coating, on the other hand, is a scalable technology already adopted by industry for the deposition of transparent conductive metal oxides for numerous

applications including fuel cells and solar cells.[15] In the present study, we have chosen a formulation based on $In(NO_3)_3$ as the precursor compound and water as the solvent, as they are both inexpensive and easy to handle. The latter material combination also presents an environmentally friendly alternative to the commonly used organic solvent-based precursor formulations,[16] with positive implications to large-scale manufacturing. Moreover, precursor layers spin-coated from aqueous solution were previously shown to convert to In_2O_3 at 250 °C and successfully used in electron transporting (n-channel) TFTs with mobility of up to 14 $cm^2\,V^{-1}\,s^{-1}$ when processed at 300 °C.[17]

The quality of In_2O_3 layers grown via spray pyrolysis is known to depend on the substrate material and its temperature as well as on the precursor formulation employed.[18–22] At adequately high deposition temperatures, researchers have observed and exploited a phenomenon called the Leidenfrost effect.[23,24] The latter occurs when a liquid droplet is not touching the surface of a hot substrate (*i.e.* it "levitates") owing to an insulating vapour layer created instantly between the droplet and the substrate. Although Leidenfrost mediated material deposition was reported previously, still significant lack in the understanding of the exact deposition mechanism exists primarily due to many non-equilibrium processes occurring simultaneously during layer nucleation and growth. To the best of our knowledge, a systematic study of the nucleation and growth of low-dimensional In_2O_3 layers at different deposition temperatures via spray pyrolysis has yet to be reported. Here we study the dynamic and thermal interactions between the heated substrate and aqueous precursor solution droplets formed during ultrasonic spraying and we demonstrate the importance of the Leidenfrost effect for the growth of highly uniform and crystalline In_2O_3 layers at temperatures in the range 240–300 °C. We show that In_2O_3 TFTs prepared via ultrasonic spray pyrolysis clearly benefit from the Leidenfrost effect with the resulting transistors exhibiting maximum electron mobility values of up to ~40 $cm^2\,V^{-1}\,s^{-1}$, at a process temperature of 252 °C, and 26 $cm^2\,V^{-1}\,s^{-1}$ at the reduced temperature of 240 °C. Key to this success is the formation of highly crystalline In_2O_3 layers

via a vapour phase mediated growth process closely resembling that of chemical vapour deposition (CVD).

2. Growth of In$_2$O$_3$ layers via spray pyrolysis

2.1. Liquid droplet-substrate interaction at different temperatures

Interactions between liquid droplets and hot substrates are typically investigated using high-speed cameras.[25–29] In the present study, however, the very small droplets sizes and short impact interval renders the use of high-speed cameras impossible. Instead, we have chosen to study the drying patterns of the individual droplets following spray deposition. Specifically, by reducing the precursor solution feed rate through the ultrasonic nozzle, we have been able to deposit spatially separated droplets and study them individually. The ultrasonic spray coating system employed allows formation of droplets with sufficiently narrow diameter distribution and a mean value of 55 (±15) µm (see *Supplementary information*).

First, we investigated the interaction between the droplet and the substrate at different hotplate temperatures. **Figure 1** shows optical (top row) and scanning electron microscopy (SEM) images (middle row) of the dried patterns of individual droplets taken after deposition onto Si^{++}/SiO$_2$ substrates maintained at different temperatures. The variation of the dried droplet shape as a function of temperature reveals a distinct change at temperatures between 203 and 271 °C with droplets processed at lower temperatures being pinned to the substrate at the edges and droplets sprayed at higher temperatures tending to split into smaller droplet-beads. The height profile of each droplet's drying pattern, measured by profilometry and/or atomic force microscopy (AFM), is shown in the bottom row of **Figure 1**. Evidently, upon impingement, all pinned droplets dry and exhibit the coffee-ring effect (*i.e.* the solute accumulates at the edges of the drying droplet)[30] with the coffee-ring height decreasing with increasing hotplate temperature.

In order to demarcate as well as quantify the transition between the low and the high temperature deposition regimes, we have defined two characteristic features associated with the formed droplet patterns: (i) the average pinned droplet diameter denoted as D_{AVG}, and (ii) the average maximum height of the coffee-ring, denoted as H_{AVG} (see **Figure 1**). The temperature dependence of D_{AVG} and H_{AVG} are shown in **Figure 2** and can be divided into three temperature regions namely: nucleate boiling (NB), transition boiling (TB), and Leidenfrost boiling (LB).[31,32] NB is the type of boiling that occurs when the hotplate temperature is higher than the boiling temperature of the liquid, but the heat flux allows liquid to wet the substrate. In the TB regime, formation of significant vapour during heating of the droplet occurs making it difficult for the liquid to wet the substrate surface. In the LB temperature region, the vapour surrounding the droplet increases further forming an insulating layer between the heated substrate and the droplet, which further suppresses wetting. This makes the liquid droplet hover over the substrate and prevents it from boiling rapidly. Detailed discussion of the heat transfer interactions between the arriving liquid droplets and the heated substrate surface is given in **Section S1** in the *Supporting Information* with **Figure S1** showing a cartoon of the step-by-step evolution of droplet-hot surface interaction and subsequent In_2O_3 deposition.

Evidently, in our system NB is taking place at $T < 200\,°C$, TB at $200 \leq T \leq 250\,°C$ and the Leidenfrost effect dominated boiling (LEDB) occurs at $T > 250\,°C$ (**Figure 2**). We note that the LEDB regime cannot be called LB since some wetting of the droplet-beads is observed and should be completely absent in the case of conventional Leidenfrost effect.[27] The Leidenfrost transition temperature of ~250 °C nearly coincides with the literature data for water-aluminium, water-stainless steel and water-Si^{++}/SiO_2 systems.[23,32] The NB and LEDB regimes are characterised by the relative independence of the D_{AVG} and H_{AVG} values on hotplate temperature, whereas TB is associated with the steep reduction of the magnitude of these characteristic features with increasing temperature. Specifically, upon transition from NB to LEDB, both D_{AVG} and H_{AVG} undergo a dramatic change from 50 to 1.5 µm and from 70 to 2

nm, respectively. We find that growth of In$_2$O$_3$ within the LEDB regime results in significantly smoother layers with significantly lower surface roughness. This is an important finding since defects-free semiconductor layers are often a prerequisite for reliable electronic device fabrication and operation. Since the primary aim of this work is the growth of the high quality semiconducting layers, we will only consider growth of In$_2$O$_3$ within the LEDB regime.

The impact of the different growth regimes on the chemical features of the deposited In$_2$O$_3$ layers was investigated via XPS (see *Supplementary information*). The XPS spectra revealed that apart from the adventitious carbon the only existing elements in the layers are In, O, and N (see **Section S2**, **Table S1**). The latter is due to the presence of In(NO$_3$)$_3$ residues and may indicate incomplete precursor conversion.[9] A first indication of the difference between the sample deposited in LEDB regime with those prepared in the TB regime and via spin-coating, is the [O]/[In] ratio, which is close to 1.5, thus corresponding to stoichiometric In$_2$O$_3$, for the former case and to 1.75 for the latter cases.

The chemical features of In$_2$O$_3$ were further studied by analyzing the O 1s core level spectra since they are known to be sensitive to chemical variations.[9,33,34] The O 1s envelope was deconvoluted to three individual peaks located at 529.5 eV (In−O bonds in crystalline In$_2$O$_3$), 530.2 eV (O adsorbates on the surface), and 532 eV (water and In−OH bonds in In$_2$O$_3$ defect sites) **(Figure S2)**.[33,34] The quantitative results of this deconvolution are presented in **Figure S3**. As can be seen, the spayed sample grown at 220 °C exhibits high contributions related to oxygen adsorbates and In−OH bonds, and has a remarkable resemblance with the spin-coated sample annealed at 250 °C. The high concentration of In-OH bonds is an indication of the presence of structural defects, such as grain boundaries, and of incomplete precursor conversion.[9] On the contrary, In$_2$O$_3$ layers sprayed within the LEDB regime (250 °C) exhibit sharp O 1s peak, which is dominated by the In-O bonds. Interestingly, the XPS spectra of the latter sample closely resemble those of In$_2$O$_3$ layers grown from vapour phase,[35] thus further

supporting the existence of a different solidification process. The minor contributions of In-OH

bonds and surface adsorbates to the O 1s core level spectrum of the sample grown in the LEDB

regime are attributed to small parts of the In$_2$O$_3$ layer grown from the liquid phase (**Figure 1E**).

2.2. In$_2$O$_3$ layer growth in the Leidenfrost effect dominated boiling regime

Figure 3a-c shows SEM and AFM images of dried In$_2$O$_3$ droplets on Si^{++}/SiO$_2$ wafers, while

Figure S4 displays the droplet size distribution and the impact of the substrate material and

hotplate temperature. The micrographs reveal a complex In$_2$O$_3$ layer morphology consisting of

thicker and thinner regions. Analysis of these patterns reveals that some portion of the layer is

deposited from the droplet-beads attached to substrate. The tiny (~2 µm diameter) droplet-beads

that wet the surface will quickly evaporate leaving a non-uniform 1–5 nm thick coffee ring

residues of the indium hydrate and indium oxide (**Figure 3a**, arrows pointing down-right). This

can be considered as a deposition from solution similar to drop-casting or spin-coating process

followed by a high temperature thermal annealing step.[17] On the other hand, the lighter back-

scattered electron contrast (arrows pointing down-left in **Figure 3a**) with diffused boundary

instead of the coffee-ring boundary observed in SEM images (arrows pointing up right),

indicates a different growth mechanism that does not involve contact between the droplet and

the substrate. It has been previously proposed that during LB the semiconductor layer is

deposited via the vapour layer that exists between the levitating drop and the hot substrate.[23,24]

This vapour phase mediated growth process resembles that of CVD[19] and our results appear

to support this hypothesis. However, one should be aware that during boiling of certain

solutions, *e.g.* NaCl in water, the liquid phase might evaporate faster leaving the heavy solid

solute species precipitated. To verify that this does not happen here, we have carried out a

deposition experiment where the hotplate and the spray nozzle we rotated by 90° (**Figure S5**).

This significant change in the spraying geometry is expected to alter the direction of falling

solid precipitates, if any, while keeping the direction of evaporating liquid uniform in all directions. Despite the difference, however, no obvious change in the deposited features can be observed implying that the growth of In_2O_3 occurs via the vapour phase. The AFM images in **Figure 3b-c** allow us to identify the edge of the deposited materials within the different regions of the layer, while **Figure 3d** displays a cartoon of the deposited In_2O_3 pattern with each distinct region highlighted for clarity. Line scans taken across the apparent layer boundaries (scans 1 and 2 indicated in **Figure 3b)** allows measurement of the In_2O_3 thickness deposited via the vapour phase from a single droplet yielding a value of ~0.5 nm (**Figure 3e-f**). This thickness is approximately half of the unit cell of cubic In_2O_3[36] and highlights the truly low-dimensional nature of the formed In_2O_3 layers. Based on these results we conclude that nucleation and growth of In_2O_3 layers processed via ultrasonic spray pyrolysis occurs via two main processes: (1) deposition from solution (regions indicated with circles in **Figure 3d**), and (2) deposition from a vapour phase mediated growth process indicated as the shaded area in **Figure 3d**.

Effective manifestation of the Leidenfrost effect depends on various factors such as substrate temperature, speed and size of the impinging droplet, the boiling point and latent heat of the solvent as well as the heat conductivity of the substrate (**Figure S3c**). For instance, droplets with an initial temperature much lower than their boiling point and moving with high speed will wet the hot substrate surface on impact and as such they will not experience the Leidenfrost effect. In contrast, droplets with an initial temperature close to their boiling point and with lower speed will instantaneously exhibit Leidenfrost effect.[26,27,37] In the current ultrasonic spraying system, when a water droplet approaches the surface with high speed of ~1 m s^{-1}, it retains a nearly constant temperature (*i.e.* room temperature) owing to the high specific heat capacity of water. It will therefore be expected to partially wet the substrate at the moment of impact.

At hotplate temperatures <200 °C, the droplet-substrate interaction upon spraying can be divided into two dominant effects. The first one is the impact of the droplet on the substrate,

and the second is the evaporation of the droplet. These two effects can be separated because the time it takes for the droplet to evaporate at these low temperatures is larger than the droplet recoil time, *i.e.* the time between the moment of impact and the moment when the droplet reaches its largest spreading diameter (see *Supplementary Information*). At high hotplate temperatures, however, these time-scales become comparable (~10 µs, see *Supplementary Information*, **Section S1**) and the surface tension and the interface tension rapidly change magnitudes. Therefore, the droplet becomes unstable and disintegrates into the smaller droplet-beads (**Figure 3a-c**). Similar droplet breaking has been reported in larger and faster droplets and was ascribed to the instability of the vapour film which forms between the droplet and a surface during impact.[25,27] After the breakage of the initial droplet, the significantly smaller droplet-beads experience the Leidenfrost effect because they have now reached the boiling temperature of the solvent and their velocity in the vertical direction has been reduced dramatically. These droplet-beads can now travel freely over the surface of the substrate. It should be noted here that during this evaporation period the local substrate temperature may fall by 5 to 50 °C (depending on the droplet life-time and size),[37,38] which in some cases may be lower than the Leidenfrost temperature. This will cause the droplet to wet the surface and get pinned by its edges. Evidence of this effect are presented in **Figure 1e, Figure 3** and **Figure S6**.

The effective substrate cooling by the liquid droplets may affect the layer deposition process in several ways. First, significant substrate temperature decrease can be induced by an increased droplet flux, with the first droplets cooling the substrate and causing the next arriving droplets to wet the surface and ending up in the transition boiling or even nucleate boiling regimes (**Figure S7**). In the present system we have found that a flux below 100 drops s^{-1} mm^{-2} is the optimum for the LEDB regime. Second, the effective substrate cooling also depends on the substrate thermal properties. For example, Si^{++} wafers caped with thinner SiO$_2$ layers experience LEDB at lower temperatures due to a faster heat exchange between a heated

substrate and the arriving liquid droplet. For Si^{++} wafers with SiO_2 thickness of 50, 100 and 400 nm Leidenfrost boiling occurs at approximately 220, 225 and 250 °C respectively (**Figure S3c**). Conversely, we have not observed any Leidenfrost boiling on glass substrates for temperatures up to 315 °C owing to the low thermal conductivity of glass, which is 100 times lower than that of Si. Moreover, it has been previously reported that the Leidenfrost transition for the glass substrate/water droplet system can be only observed at temperatures above 500 °C.[32,39] This makes the growth of high quality In_2O_3 layers via spray pyrolysis on plastic and glass substrates, at low temperatures, challenging. This effect may well be responsible for the >10-fold reduction in the electron mobility measured between In_2O_3 TFT prepared on Si^{++}/SiO_2 and those on plastic substrates.[9,40]

3. Fabrication of In₂O₃ transistors via ultrasonic spray pyrolysis

The electron transport properties of In_2O_3 layers were investigated using a bottom-gate, top-contact transistor architecture. Continuous In_2O_3 layers were grown via sequential spray coating runs (or spraying cycles) at a constant droplet flux of 100 drops s^{-1} mm^{-2}. For the given deposition conditions employed here (molarity of the precursor solution, spraying geometry and raster speed of the spraying nozzle), the layer growth rate (nm per spraying cycle) was found to depend on the substrate temperature and varied between 0.04 and 0.17 nm/spraying cycle as measured by ellipsometry and AFM (**Figure S4d**). In order to ensure complete coverage of the substrate with In_2O_3, the channel thickness in all transistors studied was chosen to be between 5 and 10 nm.

Figure 4 shows the effect of hotplate temperature on the surface topography of In_2O_3 layers and TFT performance. Specifically, **Figures 4a-b** show AFM topography images of two In_2O_3 layers deposited at 245 and 291 °C, respectively. As expected from the previous discussion, In_2O_3 layers deposited above the Leidenfrost temperature at 291 °C exhibits an exceptionally smooth surface with a root-mean-square (RMS) roughness of ~1.2 nm (**Figure**

4b). The latter is over 10 times smaller than the RMS value of ~17 nm measured for the layer grown at 245 °C – below the Leidenfrost temperature (**Figure 4a**), clearly demonstrating the benefits of In_2O_3 growth within the LEDB regime.

Figure 4c shows the transfer characteristics of several In_2O_3 TFTs grown at different temperatures in the range 245–285 °C, whilst **Figure 4d** displays the extracted electron field-effect mobility (μ_{FE}), measured in saturation, and threshold voltage (V_{TH}) spreads for each process temperature. Evidently, the transistor performance increases sharply at temperatures just above 250 °C, which coincides with the onset of the Leidenfrost temperature identified in **Figure 2**. At temperatures between 265 and 300 °C the μ_{FE} remains approximately constant and in the range 30–40 $cm^2\ V^{-1}\ s^{-1}$, with the peak value of 38.5 ($\pm$1.5) $cm^2\ V^{-1}\ s^{-1}$ obtained at 265 °C. Since the layer growth rate reduces abruptly at higher temperature (**Figure S4d**), transistor channels deposited at 275 °C and 287 °C are expected to be thinner than those deposited at 265 °C. This reduced dimensionality may be partly responsible for the reduction in the performance observed in TFTs prepared at $T > 265$ °C (**Figure 4c-d**), although other factors such as layer density and stoichiometry, due to different growth dynamics, may also play important roles.[9]

To verify, but also further exploit, the Leidenfrost effect dominated growth process occurring during ultrasonic spray deposition, we have studied the influence of the substrate material system on the temperature at which the LEDB effect occurs. This was achieved by reducing the thickness of SiO_2 from 400 nm to 100 nm. Such change is expected to cause the LEDB to occur at significantly lower temperatures due to the faster heat exchange between the substrate (Si^{++}/SiO_2) and the arriving liquid precursor droplets, in agreement with the experimental observations presented in **Figures S4c** and the AFM data in **Figure S8**. **Figure 5a** displays the evolution of the μ_{FE} *vs.* hotplate temperature for two sets of In_2O_3 TFTs prepared on Si^{++} wafers with 100 nm SiO_2 (set 1, **Figure 5a** - circles) and 400 nm-thick SiO_2 (set 2,

Figure 5a - squares). Evidently, the μ_{FE} for In_2O_3 TFTs based on the 100 nm SiO_2 reaches maximum values close to 40 $cm^2 V^{-1} s^{-1}$ for a process temperature as low as 252 °C. This is an intriguing finding and demonstrates the potential of spray pyrolysis as a scalable deposition method for the development of next generation metal oxide TFTs.

The results presented so far reveal that deposition of In_2O_3 via spray pyrolysis is due two distinct growth mechanisms, namely: (1) deposition from solution, and (2) deposition from vapour due to the LEDB effect. To investigate whether the benefits associated with the LEDB effect observed at higher deposition temperatures are unique to spray pyrolysis, we prepared two additional transistor sets; one from solution deposited via conventional spin coating and one by spray pyrolysis employing the same aqueous indium nitrate precursor formulation (see *Experimental*). Both samples were subjected to the same temperature of 255 °C either via a post-deposition thermal annealing step (for spin coated layers) or during ultrasonic spraying (pyrolysis). The thickness of the spin-coated film was approximately 4 nm. **Figure 5b** shows the transfer characteristics measured in saturation ($V_D = 40$ V) for the two devices. Evidently, spin coated In_2O_3 TFT exhibit much lower electron mobility with a maximum value of ~5 $cm^2 V^{-1} s^{-1}$ (**Figure 5b**). Transistors prepared via spray pyrolysis, on the other hand, exhibit superior performance with average μ_{FE} of 38 (±2) $cm^2 V^{-1} s^{-1}$. The high OFF-current in the spin-coated samples is caused by the lateral gate-leakage through the un-patterned In_2O_3 film.

To elucidate the origin of the large difference in μ_{FE}, we have studied the microstructure of the spin-coated and sprayed In_2O_3 layers using grazing incidence x-ray diffraction (GID) and high-resolution transmission electron microscopy (HRTEM) measurements. **Figure 6** displays the diffraction spectra measured for the two ultra-thin In_2O_3 layers. Analysis of the diffractograms reveal that spray-coated layers exhibit significantly higher crystallinity when compared to spin-coated ones. Moreover, indexing of the various peaks indicate that the sprayed layer is dominated by the polycrystalline cubic In_2O_3 phase with lattice constant of 10.6

($\pm$0.3) Å.[9] Spin coated In_2O_3 exhibit similar diffraction peaks but with significantly less well-defined features indicative of a lower degree of crystallinity.

These findings were readily confirmed by HRTEM in conjunction with fast Fourier Transform (FFT) analysis. **Figure 7** illustrates HRTEM images of a sprayed (**Figure 7a**) and a spin-coated (**Figure 7b**) In_2O_3 layers grown at 250°C, respectively, viewed edge-on. The former is a 11.5 ($\pm$ 1) nm thick uniform film, consisting of successive In_2O_3 single crystals 10-30 nm long across the lateral direction, thus exhibiting a quadrilateral platelet-like form. Although textured growth of a crystalline material on an amorphous substrate is unlikely, our analysis revealed that In_2O_3 crystals are predominantly oriented parallel to the [110] projection direction with minor in-plane rotations and out-of-plane tilts within 5° about the [001] growth axis (**Figures 7a** and **S9**). Conversely, the 2.8 ($\pm$0.3) nm thick spin-coated In_2O_3 film comprises a blend of randomly oriented nanocrystals with 2-5 nm lateral dimensions, along with residual crystalline nuclei embedded in amorphous In_2O_3 (**Figure 7b**). The interfaces between the In_2O_3 crystalline layers and the 100 nm thick SiO_2 amorphous substrate are relatively sharp, where In_2O_3 follows the nanoscale (1.5 nm) surface roughness of the substrate. Although there is no periodic structural interface between In_2O_3 and SiO_2, their bonding appears to be cohesive and no delamination is observed. Moreover, In_2O_3 layers sprayed below the Leidenfrost transition temperature (for the specific SiO_2 thickness ~225°C) appear nanocrystalline and composed of 3-6 nm in diameter spheroidal nanocrystals with no preferential orientation (**Figure S10**).

Consequently, we conclude that the dramatically enhanced layer crystallinity and accompanied transistor performance is due to the CVD-like growth of the In_2O_3 occurring upon contact of the precursor droplets with the heated substrate. Our results also suggest that it is the Leidenfrost temperature that matters the most with the actual substrate temperature playing a secondary role. Finally, it can be concluded that the regions of the In_2O_3 layer deposited from solution most likely have an adverse effect on the long-range electron transport and hence μ_{FE}.

Therefore, supressing liquid phase deposition and simultaneously increasing the vapour phase growth process, may lead to further significant improvements in transistor performance.

4. Conclusions

We studied the nucleation and growth of ultra-thin In_2O_3 layers processed via ultrasonic spray pyrolysis from an aqueous precursor solution at different temperatures. Depending on the substrate system and processing temperature, a strong influence of the Leidenfrost effect on the quality of the deposited In_2O_3 layer was observed. Experimental results revealed that formation of In_2O_3 above the Leidenfrost temperature is governed by two distinct deposition processes that occur simultaneously, namely: (i) growth from liquid phase, and (ii) growth from vapour phase due to the Leidenfrost effect. The temperature at which the Leidenfrost effect occurs was shown to depend directly on the substrate material/system itself. Specifically, for In_2O_3 layers deposited on Si^{++} wafers capped with a 400 nm thick SiO_2 layer, the optimum hotplate temperature was ~265 °C since the resulting TFTs exhibited the maximum electron mobility value of ~40 $cm^2 V^{-1} s^{-1}$. Reducing the SiO_2 layer thickness to 100 nm was shown to reduce this temperature to ~252 °C, with the maximum μ_{FE} value maintained at ~40 $cm^2 V^{-1} s^{-1}$. Even In_2O_3 TFTs processed at 240 °C exhibit exceptional performance with an average μ_{FE} of ~26 $cm^2 V^{-1} s^{-1}$, clearly highlighting the tremendous benefits associated with the vapour phase-mediated material growth process due to the Leidenfrost effect. The level of transistor performance, and particularly μ_{FE}, achieved here is significantly higher than previously reported values for In_2O_3 TFTs prepared by spray pyrolysis at similar temperatures [9] and on the same order of magnitude with the Hall mobility for In_2O_3 layers grown via spray pyrolysis at 400 °C.[13] Moreover, the obtained μ_{FE} is higher than In_2O_3 TFTs prepared by spin-coating at 300 °C,[8,10,16,17,41] outperformed only by values reported for In_2O_3 TFTs deposited on the Al-OH terminated AlO_x dielectric.[42] Finally, we believe that the Leidenfrost-mediated CVD-like

growth is applicable to different material precursors, and more generally precursor formulations (e.g. based on lower boiling point solvents), and that could one day facilitate further reduction in the process temperature with simultaneous gains in device performance.

5. Experimental

Precursor solution preparation: Indium oxide precursor solution was prepared by dissolving $In(NO_3)_3 \cdot xH_2O$ (Indium Corporation, 30 mg) in DI water (1 ml). The solution was vigorously stirred for 30 minutes to reach full dissolution. Solution was then used for the spray coating process for maximum time of 2 hours.

Indium oxide layer deposition: Degenerately doped silicon substrates with thermally grown silicon oxide of thickness between 50 and 400 nm (Active Business Company GmbH), diced into 2 cm squares, were cleaned by 10 minutes of ultrasonication consecutively in acetone and 2-propanol and dried under N_2 flow. All substrates were subjected to UV-ozone cleaning for 15 minutes to remove organic residuals and improve the wettability, which was important for spin-coating process. A SonoTek spray-coating system with 25 kHz ultrasonic frequency and power of 4 W was used for film deposition. For the TFT devices shown in this work, the solution feed rate was 0.5 ml min^{-1}, the distance between the nozzle and the substrate 13 cm, the speed of the nozzle 100 mm s^{-1} and the rastering step 10 mm. The semiconductor film deposition was carried out through a shadow mask of straight lines of 1 mm width and 15 mm length to pattern the semiconductor. The spraying area was 6×6 cm^2, although potentially it could be increased to 30×30 cm^2. For the droplet morphology studies, one pass of the spray was carried out to minimise the droplet number. The hotplate temperature had some spatial non-uniformity of maximum 2%, although the samples in this study were kept at the fixed position with temperature non-uniformity of less than 1%. The time of exposure to the temperature of all the samples was kept approximately the same between 6.5 and 7.5 minutes. In order to prepare

In_2O_3 layers entirely from liquid phase, precursor solution was spin-coated on the Si/SiO$_2$(100 nm) substrate with rate 4000 rpm for 30 s and subsequently annealed on the hotplate for 30 minutes. This resulted in the formation of approximately 4 nm-thick layers.

Thin film transistor fabrication: After semiconductor film deposition (either by spray or spin-coating), the drain-source contacts were deposited by thermal evaporation of Aluminium through the shadow mask. The TFT channel width was 1 mm, the channel length was 100 µm. The back-gate silicon was contacted by touching the exposed silicon on the side of the substrate or by scratching the top SiO$_2$ layer with the diamond pen. TFTs were measured by Agilent B2902A semiconductor parameter analyser. Charge carrier mobility was evaluated based on the gradual channel approximation:

$$\mu = \frac{\partial I_{D(linear)}}{\partial V_G} \times \frac{L}{WC_G V_D} \tag{1}$$

where $I_{D(linear)}$ is source drain current, V_G gate voltage, V_D source-drain voltage, L channel length, W channel width and C_G capacitance of a SiO$_2$ insulator. The spin-coated layers were not patterned thus resulting in the high gate-leakage due to lateral parasitic conduction.

Structural characterisation of indium oxide layers: Layer nucleation was studied using a Nikon Eclipse LV100 Optical Microscope and a Leo 40VP Scanning electron microscope with 5 kV energy electron beam and back-scattered electron sensor. The topography was studied with an Agilent 5500 atomic force microscope (AFM) operating in tapping mode. The height profiles of dried indium oxide droplets were measured using a Bruker Dektak profilometer. Film thickness was determined using different methods including, etching of the In_2O_3 layer and measuring the edge profile of the layer using either the Dektak profilometer or the AFM or by Woolam VASE ellipsometer. The model used in ellipsometry measurements was corrected using the known thickness inferred from the AFM/ profilometer measurements.

Transmission Electron Microscopy: the morphological characteristics, local nanostructure and crystallographic data of selected samples were explored by high-resolution transmission electron microscopy (HRTEM) on a Jeol 2011 UHR electron microscope operated at 200 kV. Cross-sectional HRTEM samples were prepared by the standard sandwich technique, followed by tripod polishing to reach a 30 nm edge thickness. Electron transparency to less than 12 nm was reached by low-voltage (5 to 1 keV) Ar^+ precision ion-milling in a Gatan PIPS.

Grazing Incident Diffraction Measurements: Grazing incident diffraction and X-ray reflectivity were carried out on beamline G2 at Cornell High Energy Synchrotron Source (CHESS), Cornell University. The thin films samples were aligned on a Kappa diffractometer with the X-ray energy of 11.56 keV ($\lambda = 1.073$ Å) through a Be single-crystal monochromator. The data were collected using a 640-element 1D diode-array detector, with a set of 0.1° Soller slits mounted on the detector arm to provide an in-plane resolution of 0.16°. The grazing incident angle was fixed at 0.15° in GID, except noted angles. The GID data set was integrated from 0.1° to 2° on the linear detector. The lattice constant was calculated using Bragg's law and by averaging values obtained from the reflections (222), (400), (431), (440) and (622) assuming cubic crystal structure of In_2O_3.

Supporting Information
Supporting Information is available from the Wiley Online Library or from the author.

[1]   K. Nomura, H. Ohta, A. Takagi, T. Kamiya, M. Hirano, and H. Hosono, *Nature* **2004**, *432*, 488.

[2]   E. Fortunato, P. Barquinha, and R. Martins, *Advanced Materials* **2012**, *24*, 2945.

[3]   X. Yu, T. J. Marks, and A. Facchetti, *Nat. Mater.* **2016**, *15*, 383.

[4]   L. Petti, N. Münzenrieder, C. Vogt, H. Faber, L. Büthe, G. Cantarella, T. D. Anthopoulos, and G. Tröster, *AIP Appl. Phys. Rev.* **2016**, *3*, 021303.

[5]   O. Bierwagen and J. S. Speck, *Appl. Phys. Lett.* **2010**, *97*, 3.

[6]   Z. Galazka, R. Uecker, and R. Fornari, *J. Cryst. Growth* **2014**, *388*, 61.

[7]   R. L. Weiher, *J. Appl. Phys.* **1962**, *33*, 2834.

[8]   S. Y. Han, G. S. Herman, and C. H. Chang, *J. Am. Chem. Soc.* **2011**, *133*, 5166.

[9]   H. Faber, Y.-H. Lin, S. R. Thomas, K. Zhao, N. Pliatsikas, M. A. McLachlan, A. Amassian, P. A. Patsalas, and T. D. Anthopoulos, *ACS Appl. Mater. Interfaces* **2015**, *7*, 782.

[10]   Y.-H. Kim, J.-S. Heo, T.-H. Kim, S. Park, M.-H. Yoon, J. Kim, M. S. Oh, G.-R. Yi, Y.-Y. Noh, and S. K. Park, *Nature* **2012**, *489*, 128.

[11]   J. Leppäniemi, O. Huttunen, H. Majumdar, and A. Alastalo, *Adv. Mater.* **2015**, *27*, 7168.

[12]   T. T. Baby, S. K. Garlapati, S. Dehm, M. Ha, R. Kruk, and H. Hahn, *ACS Nano* **2015**, *9*, 3075.

[13]   J. Joseph Prince, S. Ramamurthy, B. Subramanian, C. Sanjeeviraja, and M. Jayachandran, *J. Cryst. Growth* **2002**, *240*, 142.

[14]   J. S. Lee, Y. Kwack, and W. Choi, *ACS Appl. Mater. Interfaces* **2013**, *5*, 11578.

[15]   Sono-tek, "SonoTek. Customer Reviews," http://www.sono-tek.com/customer-testimonials/, accessed: November 2016.

[16]   G. Liu, A. Liu, H. Zhu, B. Shin, E. Fortunato, R. Martins, Y. Wang, and F. Shan, *Adv. Funct. Mater.* **2015**, *25*, 2564.

[17]   Y. Hwan Hwang, J.-S. Seo, J. Moon Yun, H. Park, S. Yang, S.-H. Ko Park, and B.-S. Bae, *NPG Asia Mater.* **2013**, *5*, e45.

[18]   U. P. Muecke, N. Luechinger, L. Schlagenhauf, and L. J. Gauckler, *Thin Solid Films* **2009**, *517*, 1522.

[19]   J. C. Vigui and J. Spitz, *J. Electrochem. Soc.* **1975**, *122*, 585.

[20]   M. Ortel, Y. S. Trostyanskaya, and V. Wagner, *Solid. State. Electron.* **2013**, *86*, 22.

[21]   A. Bashir, P. H. Wöbkenberg, J. Smith, J. M. Ball, G. Adamopoulos, D. D. C. Bradley, and T. D. Anthopoulos, *Adv. Mater.* **2009**, *21*, 2226.

[22] G. Adamopoulos, A. Bashir, S. Thomas, W. P. Gillin, S. Georgakopoulos, M. Shkunov, M. A. Baklar, N. Stingelin, R. C. Maher, L. F. Cohen, D. D. C. Bradley, and T. D. Anthopoulos, *Adv. Mater.* **2010**, *22*, 4764.

[23] M. Ortel and V. Wagner, *J. Cryst. Growth* **2013**, *363*, 185.

[24] U. P. Muecke, G. L. Messing, and L. J. Gauckler, *Thin Solid Films* **2009**, *517*, 1515.

[25] M. Khavari, C. Sun, D. Lohse, and T. Tran, *Soft Matter* **2015**, *11*, 3298.

[26] Y. M. Qiao and S. Chandra, *Int. J. Heat Mass Transf.* **1996**, *39*, 1379.

[27] M. Shirota, M. A. J. Van Limbeek, C. Sun, A. Prosperetti, and D. Lohse, *Phys. Rev. Lett.* **2016**, *116*, 064501.

[28] T. Tran, H. J. J. Staat, A. Prosperetti, C. Sun, and D. Lohse, *Phys. Rev. Lett.* **2012**, *108*, 036101.

[29] W. Zhang, T. Yu, J. Fan, W. Sun, and Z. Cao, *J. Appl. Phys.* **2016**, *119*, 114901.

[30] R. D. Deegan, O. Bakajin, T. F. Dupont, G. Huber, S. R. Nagel, and T. A. Witten, *Nature* **1997**, *389*, 827.

[31] C. T. A. S. Chandra, *Proc. R. Soc. Lond. A* **1991**, *234*, 13.

[32] K. J. Baumeister and F. F. Simon, *Trans. ASME* **1973**, *95*, 166.

[33] C. D. Wanger, W.M. Riggs, L.E. Davis, J.F. Moulder, G.E. Muilenberg, Handbook of X-ray Photoelectron Spectroscopy, Perkin-Elmer Corp. Physical Electronics Division: Eden Prairie, MN (1979).

[34] K.L. Purvis, G. Lu, J. Schwartz, S.L. Bernasek, *J. Am. Chem. Soc.* **2000**, *122*, 1808.

[35] T.L. Barr and L.K.J Ying Li, *J Phys. Chem.* **1989**, *5*, 57464.

[36] E. J. Tarsa, J. H. English, and J. S. Speck, *Appl. Phys. Lett.* **1993**, *62*, 2332.

[37] D. J. E. Harvie and D. F. Fletcher, *Int. J. Heat Mass Transf.* **2001**, *44*, 2643.

[38] D. J. E. Harvie and D. F. Fletcher, *Int. J. Heat Mass Transf.* **2001**, *44*, 2633.

[39] J. D. Bernardin and I. Mudawar, *J. Heat Transfer* **1999**, *121*, 894.

[40] L. Petti, H. Faber, N. Münzenrieder, G. Cantarella, P. A. Patsalas, G. Tröster, and T. D. Anthopoulos, *Appl. Phys. Lett.* **2015**, *106*, 092105.

[41] X. Yu, J. Smith, N. Zhou, L. Zeng, P. Guo, Y. Xia, A. Alvarez, S. Aghion, H. Lin, J. Yu, R. P. H. Chang, M. J. Bedzyk, R. Ferragut, T. J. Marks, and A. Facchetti, *Proc. Natl. Acad. Sci. U. S. A.* **2015**, *112*, 3217.

[42] P. K. Nayak, M. N. Hedhili, D. Cha, and H. N. Alshareef, *Appl. Phys. Lett.* **2013**, *103*, 033518.
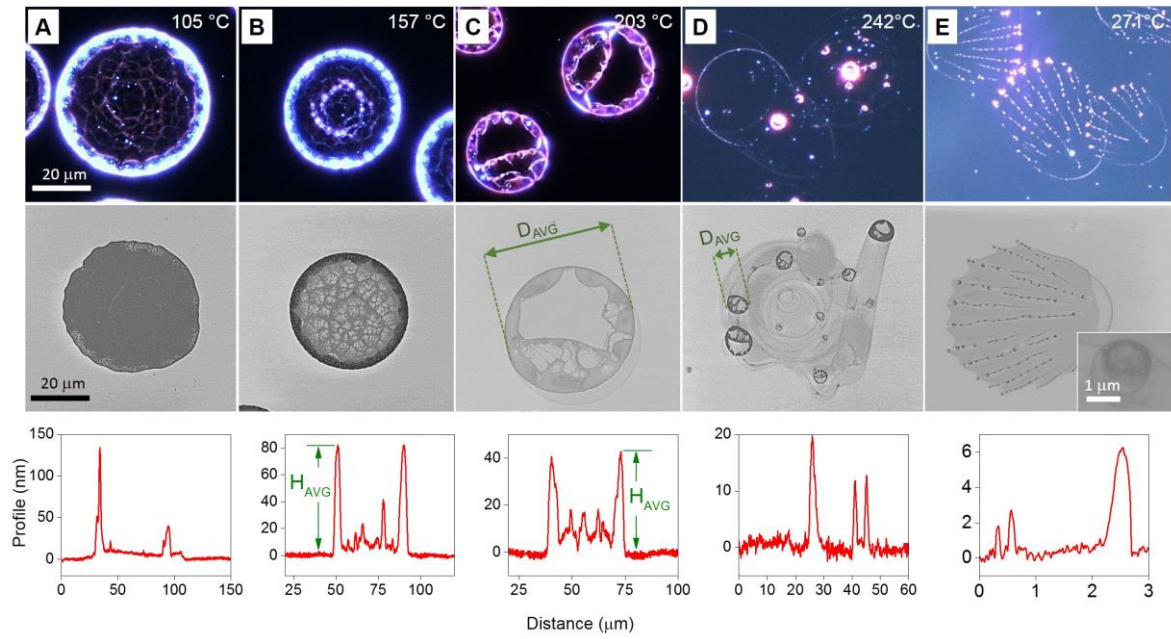
Figures

Figure 1. Optical micrographs (top row), SEM images (middle row), and the height profiles (bottom row) of the individual droplets of indium nitrate solution in water sprayed heated SiO$_2$/Si wafers at different temperatures: (a) 105 °C, (b) 157 °C, (c) 203 °C, (d) 242 °C and (e) 271 °C. The characteristic parameters namely D$_{AVG}$ for the average pinned droplet diameters, and H$_{AVG}$ for the average height of the coffee ring feature are indicated in the SEM images and height profile graphs respectively.
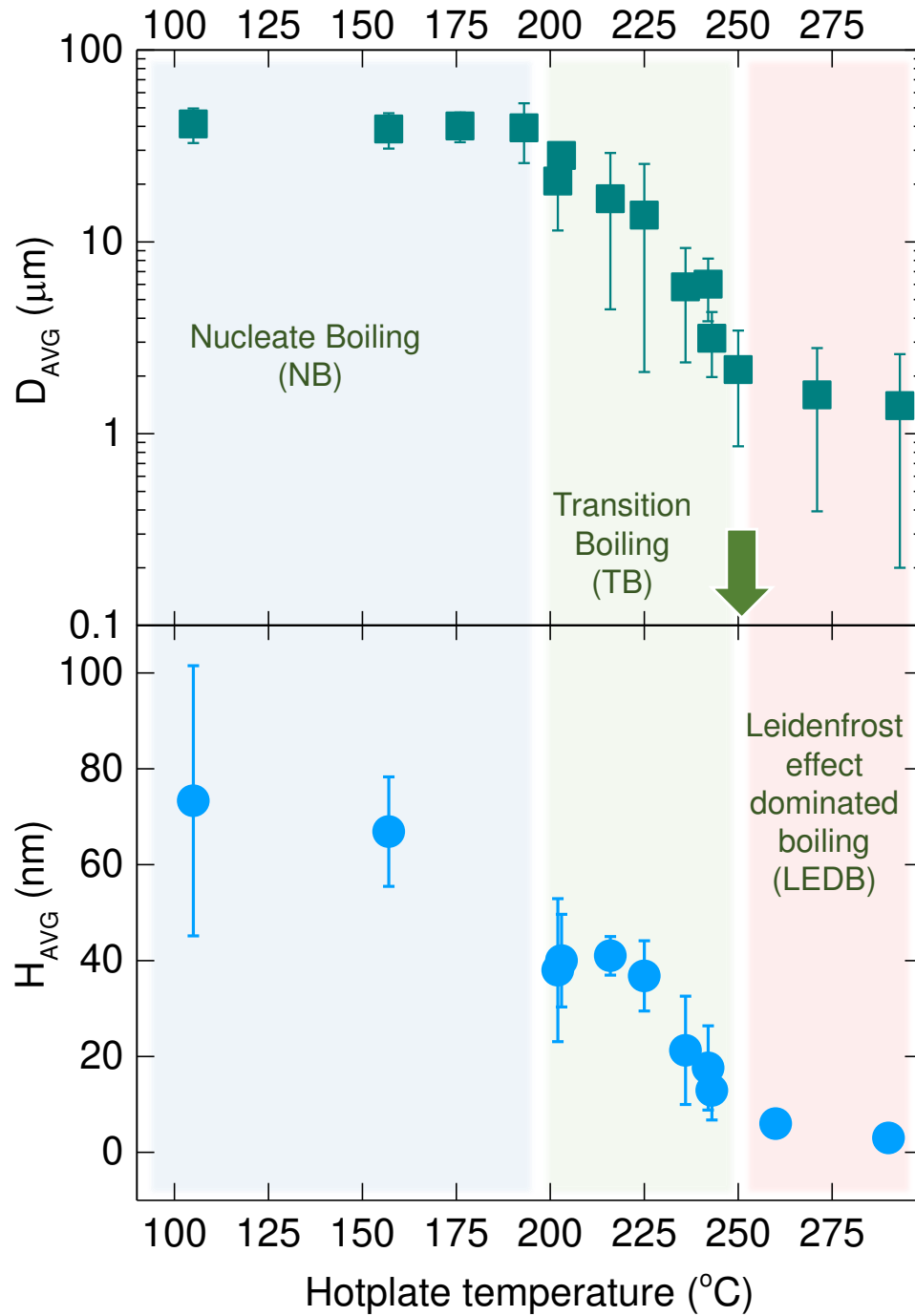
Figure 2. Temperature dependence of the average pinned droplet diameter (D_{AVG}) and average coffee-ring height (H_{AVG}). The arrow indicates the temperature at which the Leidenfrost effect occurs. For each temperature, both the diameter and height values were averaged over 100 droplets and 10 droplets respectively.
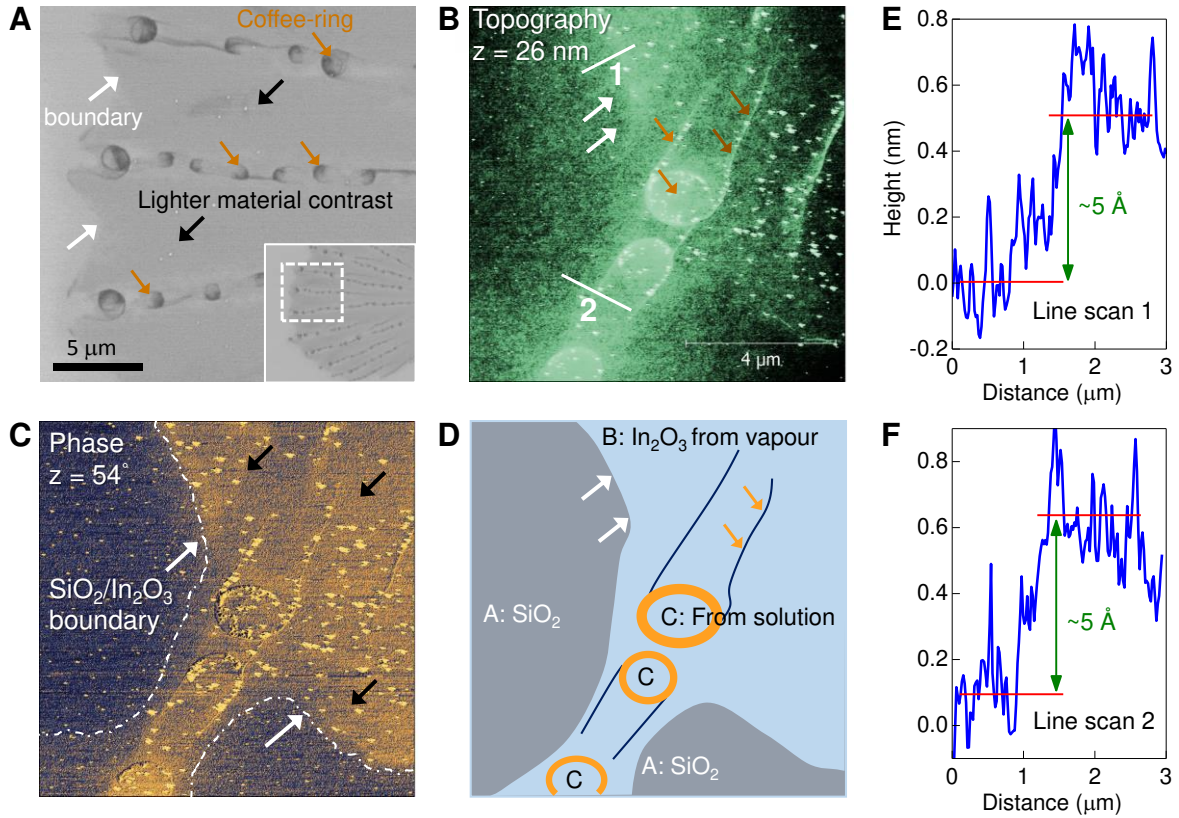
Figure 3. In$_2$O$_3$ layer deposition mechanism at 270 °C. (a) SEM image of a dried droplet side, inset: Lower magnification SEM image of the approximate area of the drop being analysed. (b) Surface topography, and (c) phase images of the boundary of a dried In$_2$O$_3$ droplet. (d) Cartoon depicting the different layer formation mechanisms at play. Arrows pointing up-right and those pointing down-left indicate the boundary between the substrate and In$_2$O$_3$ deposited via vapour phase, respectively. Arrows pointing down-right indicate regions of In$_2$O$_3$ deposited via solution phase. Panels (e) and (f) show line scans of the surface topography at positions 1 and 2 indicated in the AFM image in (b).
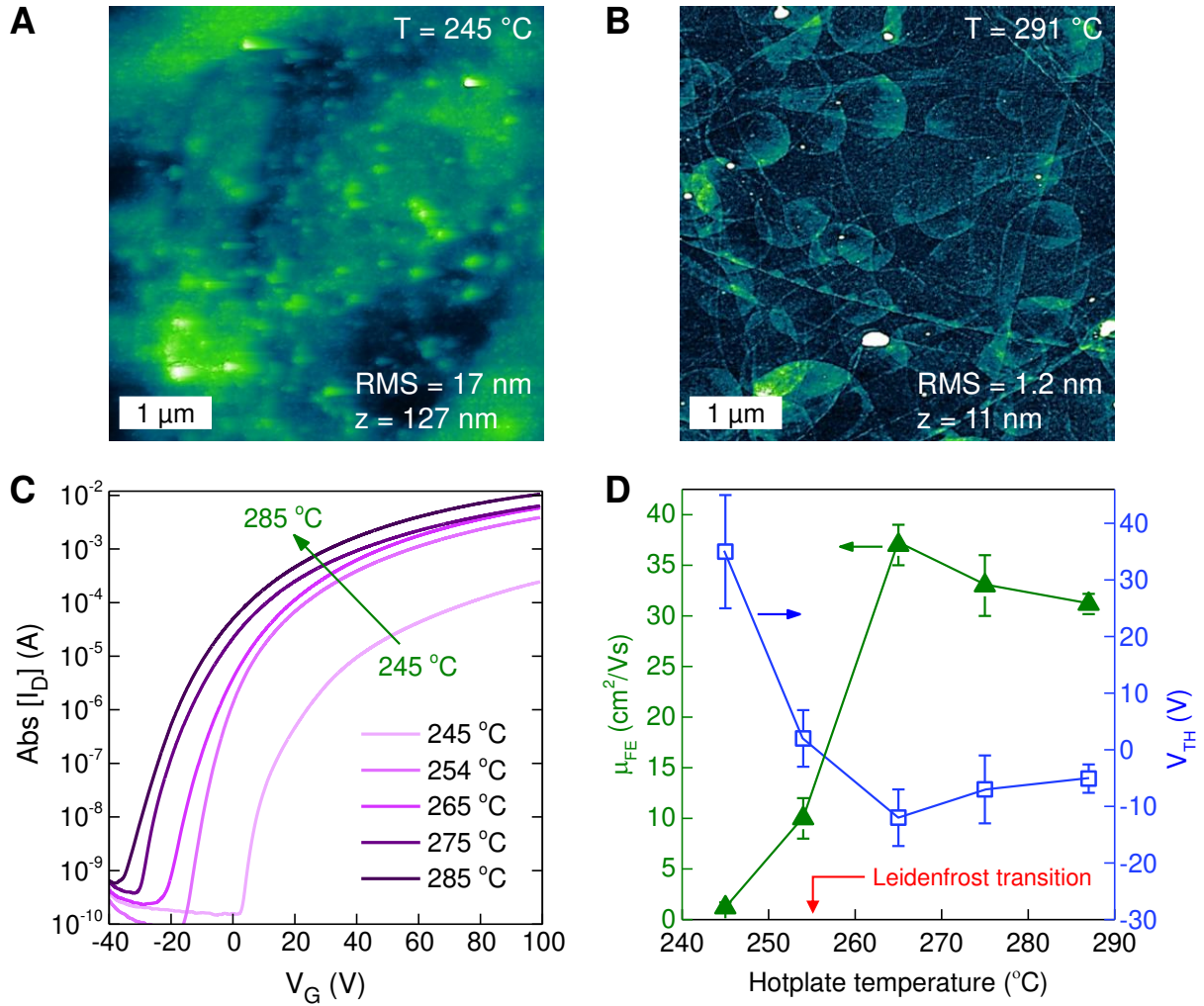
Figure 4. Topography AFM images of an In_2O_3 layers deposited at 245 °C (a), and at 291 °C (b). (c) Transfer characteristics obtained V_D = 100 V for several In_2O_3 TFTs processed at different temperatures in the range of 245 to 285 °C. All devices comprised of ~10 nm-thick In_2O_3 channel layer, 400 nm thick SiO_2 gate dielectric, with a channel length and width of 100 µm and 1000 µm, respectively. (d) Calculated values for μ_{FE} and V_{TH} as a function of process temperature.
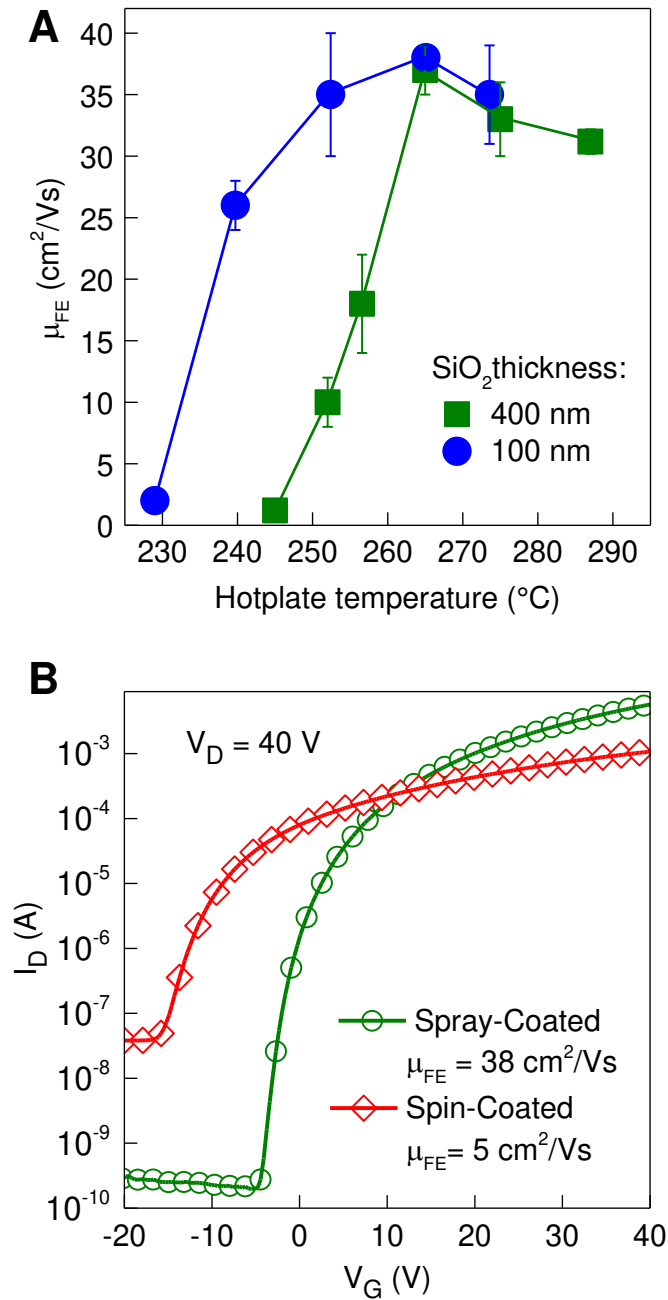
Figure 5. (a) Charge carrier mobility and threshold voltage as a function of temperature for In_2O_3 TFTs grown on Si/SiO_2 with 100 nm thick dielectric (blue circles) and 400 nm thick dielectric (green squares). (b) Comparison between the spin-coated and spray-coated TFT prepared on the same substrate (Si/SiO_2 100 nm) from the same solution at the same temperature 255 °C.
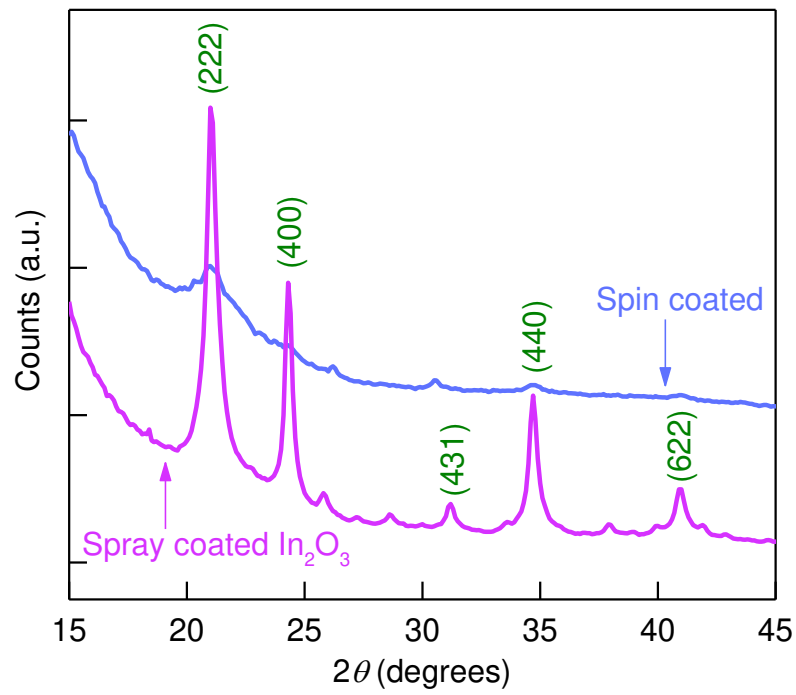
Figure 6. GID measurement carried out on the spin-coated and spray-coated In_2O_3 layers with indicated main reflections and corresponding Miller indices.
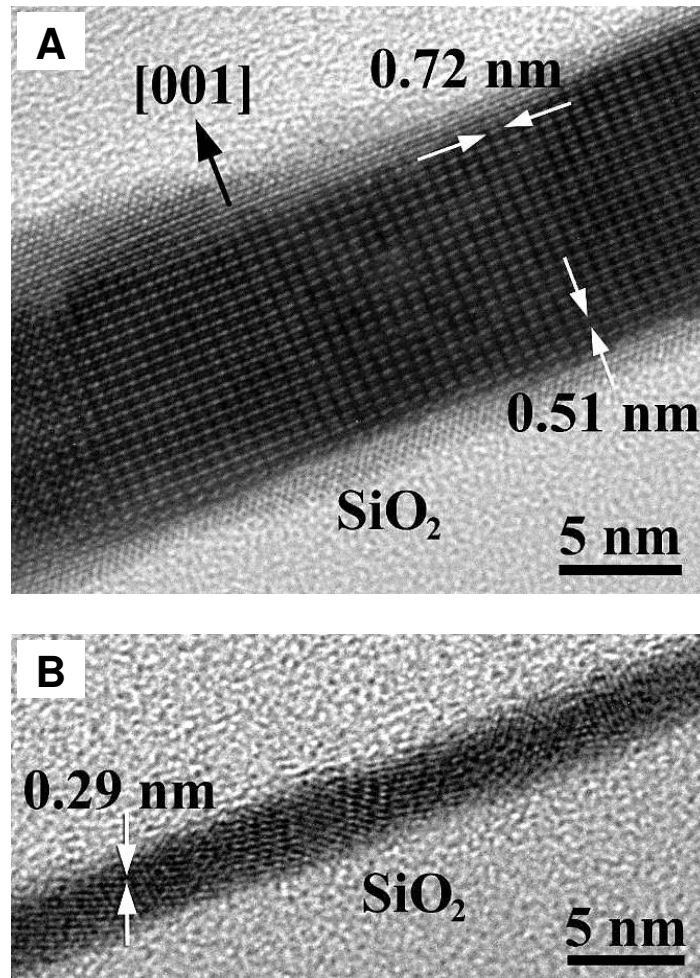
Figure 7. (a) Cross-sectional HRTEM image of an elongated single crystal, part of an In_2O_3 film sprayed on SiO_2 at 250°C, viewed edge-on. The crystal is oriented exactly parallel to the [110] projection direction, while the *d*-spacing values of its ($1\bar{1}0$) and (002) planes, 0.72 nm and 0.51 nm, respectively, are denoted by arrows. Residual In_2O_3 structure contrast projected at the interface is due to roughness of the SiO_2 surface. (b) Cross-sectional HRTEM of a nanocrystalline In_2O_3 film spin-coated on SiO_2 and annealed at 250°C, viewed edge-on. As evident, nanocrystals are randomly oriented within the film. Nonetheless, the *d*-spacing of {222} planes of the In_2O_3 cubic lattice (0.29 nm) is clearly resolved in almost all of them and is pinpointed in one for clarity (arrows).

The nucleation and growth of ultra-thin In₂O₃ layers processed via ultrasonic spray pyrolysis at temperatures in the range 100-300 °C, are studied. The Leidenfrost effect is shown to dominate material growth at processing temperatures above 252 °C leading to In₂O₃ layers with exceptional crystallinity and uniformity. Transistors based on these optimised layers exhibit remarkable electron mobility of up to 40 cm² V⁻¹ s⁻¹.

Keywords: indium oxide; spray pyrolysis; thin film transistors; Leidenfrost effect; solution processing

Ivan Isakov*, Hendrik Faber, Max Grell, Gwenhivir Wyatt-Moon, N. Pliatsikas, T. Kehagias, G. P. Dimitrakopulos, P. Patsalas, Ruipeng Li, and Thomas D. Anthopoulos*

Exploring the Leidenfrost effect for the deposition of high-quality In₂O₃ layers via spray pyrolysis at low temperatures and their application in high electron mobility transistors

ToC
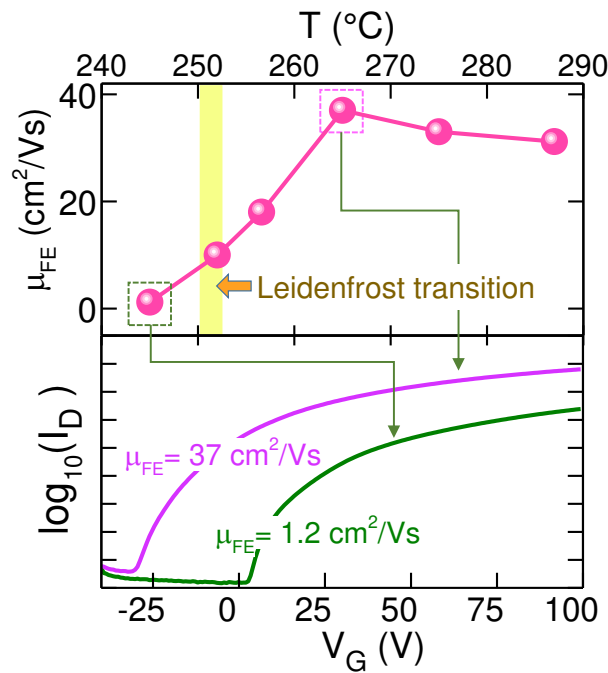
Supporting Information

Exploring the Leidenfrost effect for the deposition of high-quality In₂O₃ layers via spray pyrolysis at low temperatures and their application in high electron mobility transistors

Ivan Isakov*, Hendrik Faber, Max Grell, Gwenhivir Wyatt-Moon, N. Pliatsikas, T. Kehagias, G. P. Dimitrakopulos, P. Patsalas, Ruipeng Li, and Thomas D. Anthopoulos*

Section S1. Heat transfer

According to the simple estimation of capillary forces and surface tension,[1] the recoil time of a droplet with diameter 40 µm is approximately 30 µs with the largest spreading diameter of 50–60 µm achieved after 15 µs. The time required to heat the droplet to the boiling temperature of the solvent used and evaporate is slightly higher but of the same order of magnitude as the spreading time. These times can be calculated using the models outlined next. The heat transfer rate can be expressed as:

$$\frac{\partial J}{\partial t \partial s} = -k \nabla T \tag{SI-1}$$

where J is the heat in Joules, k is thermal conductivity (1.4 W m⁻¹ K⁻¹ for SiO₂, 0.03 W m⁻¹ K⁻¹ for air, 149 W m⁻¹ K⁻¹ for silicon and 0.6 W m⁻¹ K⁻¹ for water). For Si/SiO₂ wafers we can assume $\nabla T = (T_{Si} - T_{SiO2})/d$, where d is the thickness of SiO₂. In order to heat a 40 µm diameter droplet from a temperature of 40 °C to the boiling temperature of 100 °C, the energy needed is $J_{heat} = cm\Delta T = 7.9 \cdot 10^{-6}$ J, where c is the heat capacity (4.183 J g⁻¹ K⁻¹ for water) and m is droplet's mass. For the droplet to fully evaporate the energy needed is $J_{boil} = Lm = 8.3 \cdot 10^{-5}$ J, where L is the latent heat (2264 J g⁻¹ for water).

It is clear that for the undercooled droplet ($T < T_{boil}$) flying from the ultrasonic nozzle towards the substrate, it will take some time before it starts evaporating. Conversely, the droplet at a boiling temperature will start evaporating shortly before the moment of impact ($t = 0$ µs) and will undoubtedly experience the *Leidenfrost* effect. It is possible, however, to estimate the droplet temperature at the impact considering the initial temperature of the droplet (at the

moment when it starts its flight, *i.e.* being ejected from the nozzle), using the following equations:

$$\frac{\partial J}{\partial t \partial S} = -h\Delta T \tag{SI-2}$$

$$t_3 = \frac{cm}{Sh} \ln \frac{T_{sub} - T_{init}}{T_{sub} - T_{boil}} \tag{SI-3}$$

$$T_{drop}(t) = \left(T_{init} - T_{gas}\right) \exp\left(-\frac{Sht}{cm}\right) + T_{gas} \tag{SI-4}$$

where, h is a convection interface heat transfer coefficient. The convection interface heat transfer coefficient can be assumed to be between 20 and 300 W m^{-2} K^{-1} for water/gas interface.[2] The time t_3 to reach the boiling temperature for a spherical droplet at temperature 30 °C residing in air of 250 °C temperature appears to lie between 25 and 400 ms (the droplet is assumed to have the same mass as the one in the previous example). In our case, the droplet transits through the air at a speed of ~1 m s^{-1} and reaches the hotplate in 100 ms after detaching from the nozzle. The temperature of air through which the droplet flies is significantly less than 250 °C almost for the whole duration of the transit, moreover, it drags the cold air with it thus reducing the temperature further. Therefore, the droplet cannot reach the boiling temperature before it touches the substrate. Estimating that the only region the droplet heats up is at the height of up to 5 mm above the surface with the average temperature of the air in this area being 150 °C (this is a sensible estimation considering the literature data),[3] the droplet will heat up to a maximum of 40 °C upon reaching the substrate. In conclusion, upon impact the droplet will be below boiling temperature and it will initially, at least partially, wet the substrate.

For a sessile droplet with pinned contact line on a substrate at 250 °C, the time it takes for the droplet to reach the boiling temperature (t_1), without considering the heat transfer inside the droplet, is given by:

$$t_1 = \frac{cmd}{Sk} \ln \frac{T_{sub} - T_{init}}{T_{sub} - T_{boil}} \tag{SI-5}$$

The calculation yields a t_1 = 5.4 µs for a droplet of 25 µm radius. Due to a finite heat transfer inside the droplet, the part of the droplet in contact with the substrate will reach the boiling temperature much earlier than the top of the droplet. Whereas the time to be fully evaporated is given by:

$$t_2 = \frac{mLd}{Sk(T_{sub} - T_{boil})} \qquad\qquad \text{(SI-6)}$$

Calculations yield a value of t_2 = 58 µs. We note however that both t_1 and t_2 values should be considered as estimations and used only for comparison reasons. The main conclusion from these calculations is that the time associated with the evaporation of the droplet is much larger than time it takes to heat the droplet to the required temperature. For the same droplet impinging on a substrate maintained at a temperature of 150 °C, t_1 = 12.7 µs and t_2 = 174 µs.
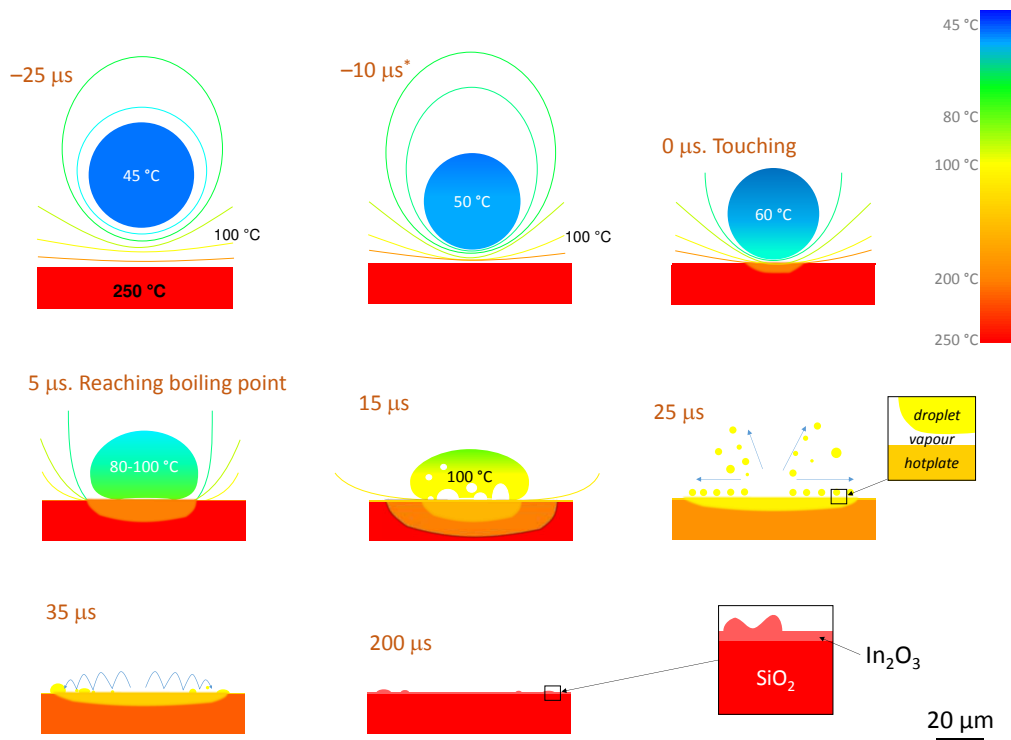
Figure S1. Cartoon showing an approximate step-by-step evolution of droplet-hot surface interaction and subsequent In$_2$O$_3$ deposition. Colour codes the temperatures of the droplet and the surface.

Section S2. Chemical Analysis

In order to further support the discrimination of the individual growth regimes at different hotplate temperatures we considered the chemical features of the deposited In_2O_3 via XPS analysis (see Figure **S1**). The XPS wide-scan spectra that correspond to In_2O_3 deposited by spray coating in the TB (220 ºC) or in the LEDB (250 °C) regime, as well as a spin-coated In_2O_3 sample at 250 ºC, have shown that apart from the adventitious Carbon the only existing elements in the layers are In, O, and N; the latter is due to residues of the $In(NO_3)_3$ precursor and might be used as an indicator of an incomplete reaction. The elemental analysis, excluding the contribution of the adventitious Carbon, is shown in Table **S1**. It is evident that in all cases there are residues of nitrogen, with the highest [N] concentration observed for the sample deposited by spray in the TB regime (220 ºC). A first indication of the difference between the sprayed sample in LEDB regime with the other two (in the TB regime and the spin-coated) is the [O]/[In] ratio, which is close to 1.5, thus corresponding to stoichiometric In_2O_3, for the former case and to 1.75 for the latter cases.

Table S1: The elemental composition of representative In_2O_3 layers.

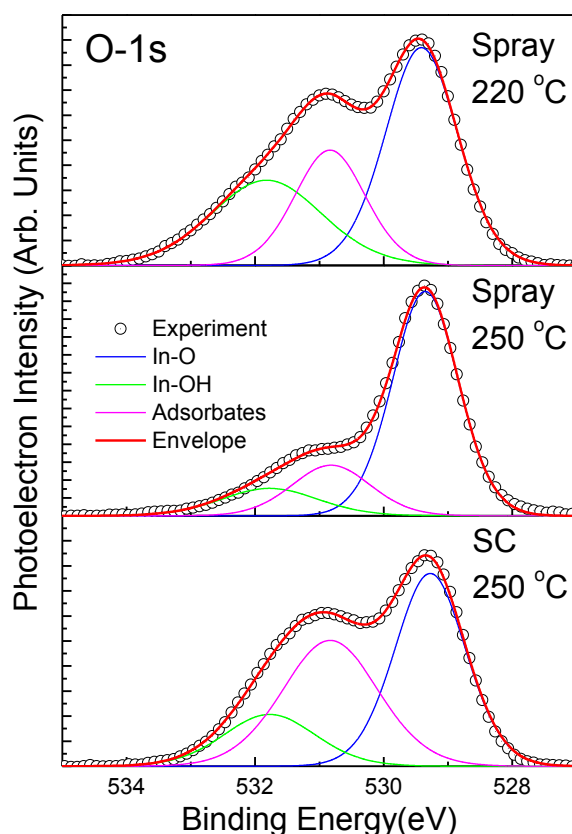|	**[O] (% at)**	**[In] (% at)**	**[N] (% at)**	**[O]/[In]**
Spray TB (220 ºC)	61.2	35.3	3.5	1.74
Spray LEDB (250 ºC)	58.5	40.0	1.5	1.46
Spin Coated (250 ºC)	63.3	35.5	1.2	1.78

Figure S2. XPS O 1s core level spectra (circles for experiment and red lines for the entire O 1s envelope) for In₂O₃ sprayed layers grown at the TB regime (220 °C, upper panel) and at the LEDB regime (250 °C, medium panel), as well as a spin-coated In₂O₃ deposited from the liquid phase at 250 °C (lower panel); the individual contributions of In-O, In-OH bonds and of O surface adsorbates are shown with blue (cantered at ~529.3 eV), green (centred at ~531.9 eV) and magenta (centred at ~530.9 eV) lines, respectively.

In order to shed more light to the chemical features of the considered In₂O₃ layers, and explain the overstoichiometry of the samples that nucleated from the liquid phase, we use the analysis of the O 1s core level spectra, as they are known to be sensitive to the chemical variations. The O 1s core level spectra corresponding to In₂O₃ deposited by spray coating in the TB (220 °C) and in the LEDB (250 °C) regime, as well as a spin-coated In₂O₃ sample at 250 °C are summarized in **Figure S1**. In all cases, the O 1s envelope can be deconvoluted to three individual peaks located at 529.5 eV (In−O bonds in crystalline In₂O₃), 530.2 eV (O adsorbates

on the surface), and 532 eV (water and In−OH bonds in In_2O_3 defect sites). The quantitative results of this deconvolution are presented in **Figure S2**.
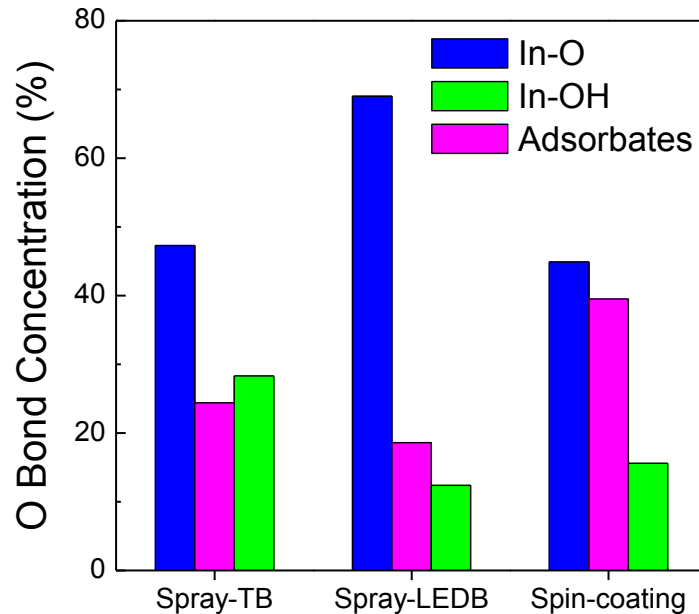

Figure S3. Histograms of the quantitative contribution of In-O, In-OH and adsorbates to the O 1s envelope for the different growth conditions.

The spayed sample grown at ~220 °C exhibits high contributions related to oxygen adsorbates and In−OH bonds, and shows a remarkable resemblance with the spin coated sample (250 °C). The high concentration of In-OH bonds indicates the presence of structural defects, such as grain boundaries, and/or incomplete chemical reaction/precursor conversion. On the contrary, the sample sprayed within the LEDB regime (250 °C) exhibits a sharp O 1s peak that is dominated by the In-O bonds and its XPS spectra strongly resembles those of In_2O_3 layers grown from the vapour phase, thus providing direct evidence of the existence of different solidification process for the LEDB regime. The minor contributions of In-OH bonds and surface adsorbates to the O 1s core level spectrum of the sample grown in the LEDB regime

are most likely attributed to material residues deposited via the liquid phase as shown in **Figure 1E**.

Section S3. Droplet kinetics

According to Wachters and Westerling,[1] the time of the impinging drop being resident on the surface before rebound is equal to the period of vibration of the freely oscillating drop (τ):

$$\tau = \pi \sqrt{\frac{\rho R^3}{2\sigma}} \tag{SI-7}$$

In the present case, the droplet is not rebounding in a common sense (i.e. like an elastic ball), thus we will only consider the time between the initial impact and the maximum spreading, *i.e.* $\tau/2$. For symmetric droplets with diameter 40 µm this time will be equal 12 µs, at 30 °C and 16 µs, at 100 °C ($\sigma_{\text{water-air}} = 0.072$ J m^{-2} at 20 °C and 0.058 J m^{-2} at 100 °C). According to our calculations, droplet impinging on a substrate at 250 °C will start boiling before it reaches the maximum spreading, whereas for a droplet impinging on a substrate at 150 °C, the droplet will reach the maximum spreading and only then will start boiling.

Next, we calculate the spreading diameter of the droplet. For a droplet flying with a speed of 1 m s^{-1}, its kinetic energy is equal to $mv^2/2$, whilst its surface energy is equal to σS. For a water droplet with a diameter of 40 µm, the surface energy is approximately 10 times larger than its kinetic energy. With all the kinetic energy being transformed into surface energy and assuming oblate elliptical deformation of the drop without substrate-liquid interaction, the larger diameter of the compressed droplet will be 50 µm and the smaller diameter will be approximately 26 µm. Existing theories [4] show that the spreading diameter is indeed between 44 and 60 µm, which coincide well with our estimation. The schematic of droplet-hotplate interaction in the current system is shown in **Figure S6**.
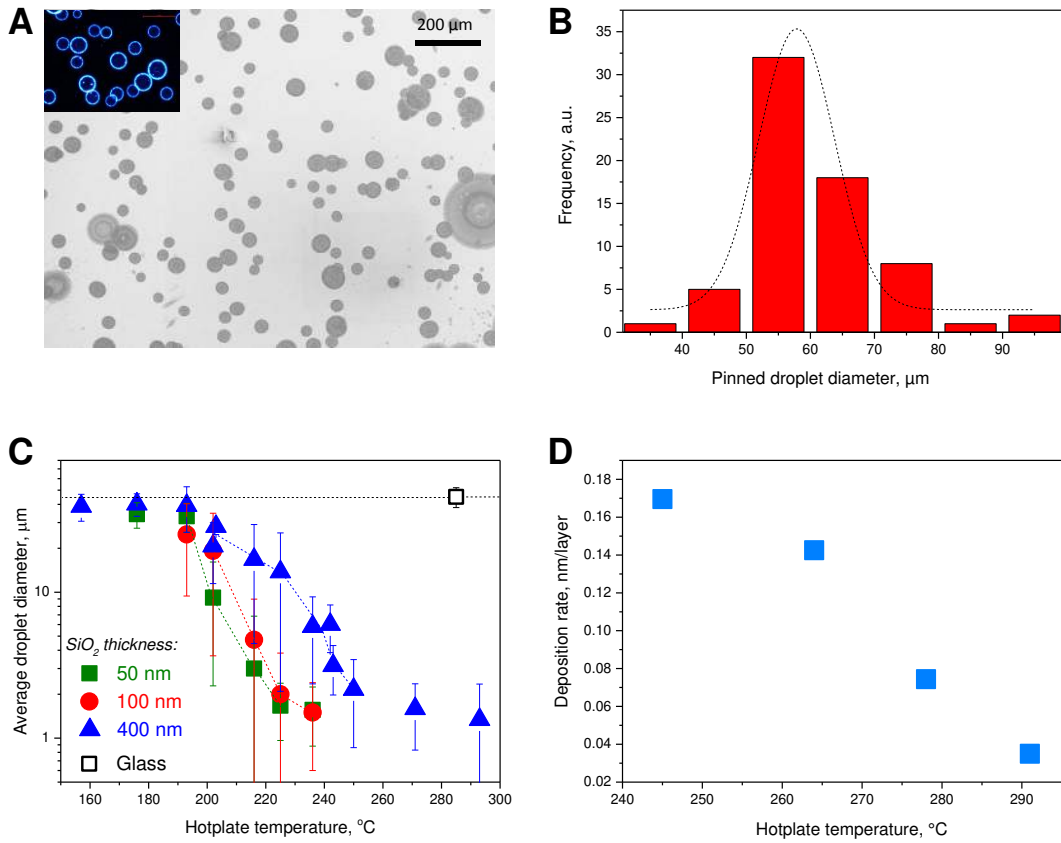
Figure S4. (a) Low resolution SEM image of the dried droplets deposited at 200 °C. Inset: Dark field optical microscopy image of the same sample with the same magnification. (b) Histogram of the measured dried droplet diameter distribution at 200 °C and Gaussian fit with mean diameter 57 µm and full width at half maximum of 15 µm. (c) Hotplate temperature dependence of the average pinned droplet diameter for droplets deposited on Si wafers incorporating SiO_2 layers of different thickness (50, 100 and 400 nm) and of glass substrate. (d) Hotplate temperature dependence of the deposition rate for Si/SiO_2 (100 nm) substrate.
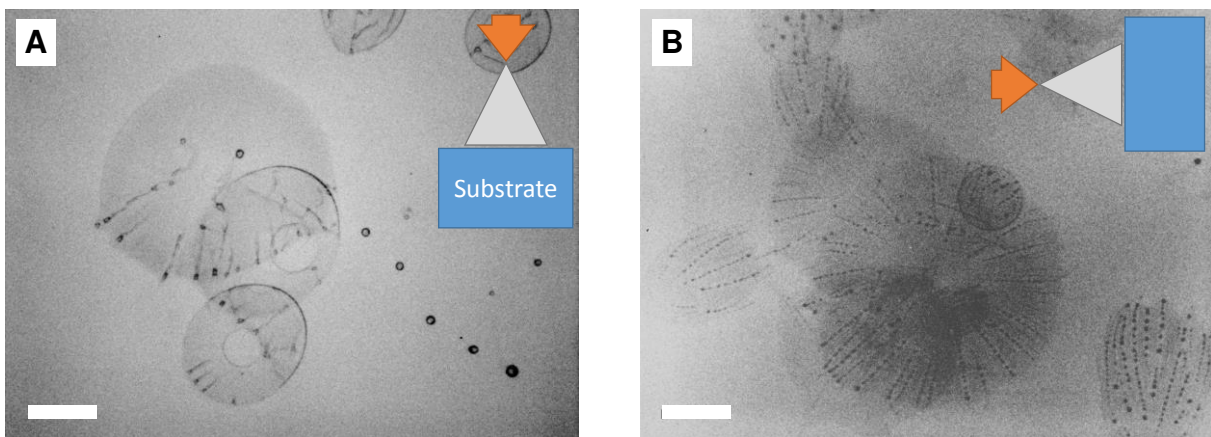
Figure S5. Optical microscopy images of In_2O_3 nucleating from the droplets impinging at different angle. (a) Gravity direction down (or normal), and (b) gravity direction rotated by 90°. Scale bars: 20 µm.
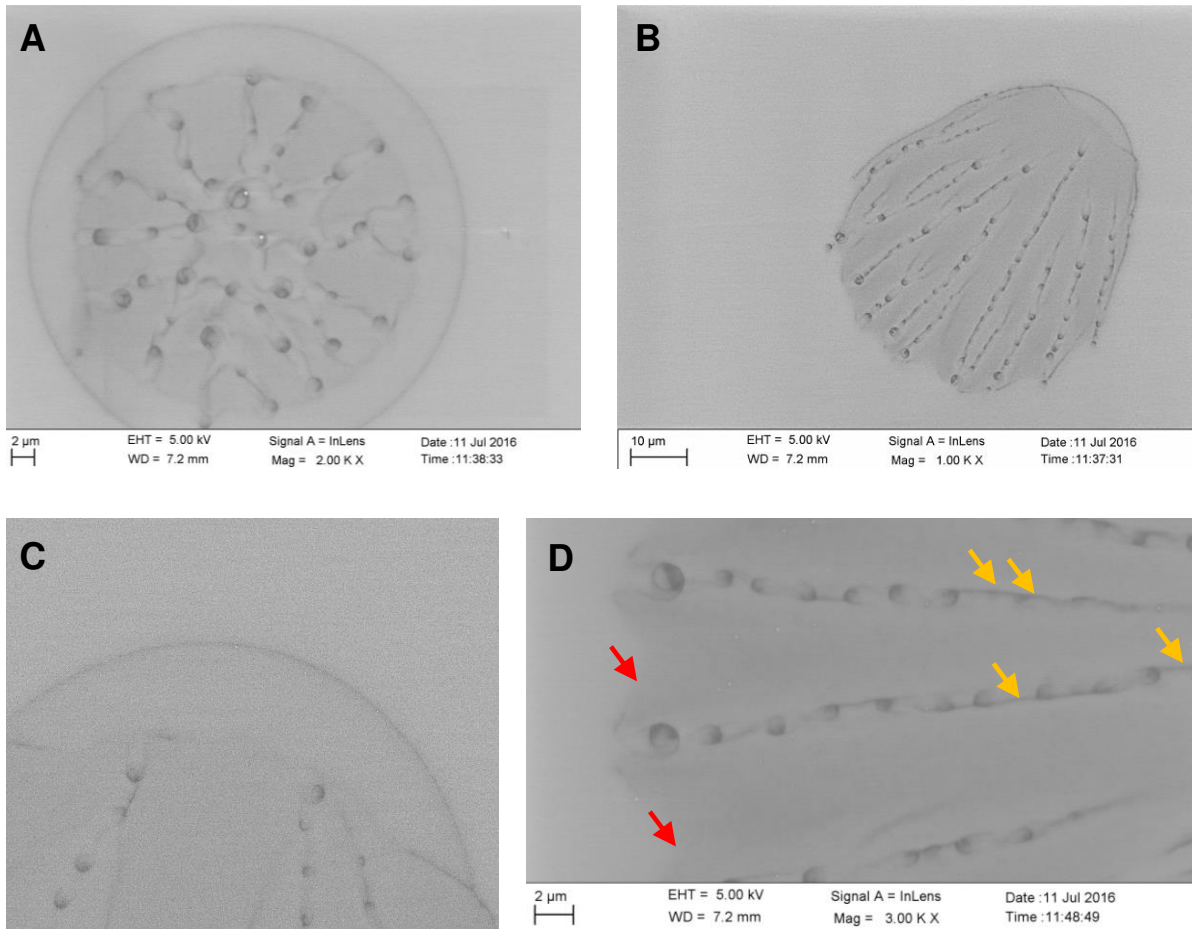
Figure S6. (a) to (d) shows SEM images of four different dried In$_2$O$_3$ droplets. Red arrows in (d) show diffused boundary of material deposited via the Leidenfrost effect-mediated deposition, while yellow arrows show places where the droplets appears to have wetted the substrate on impact.
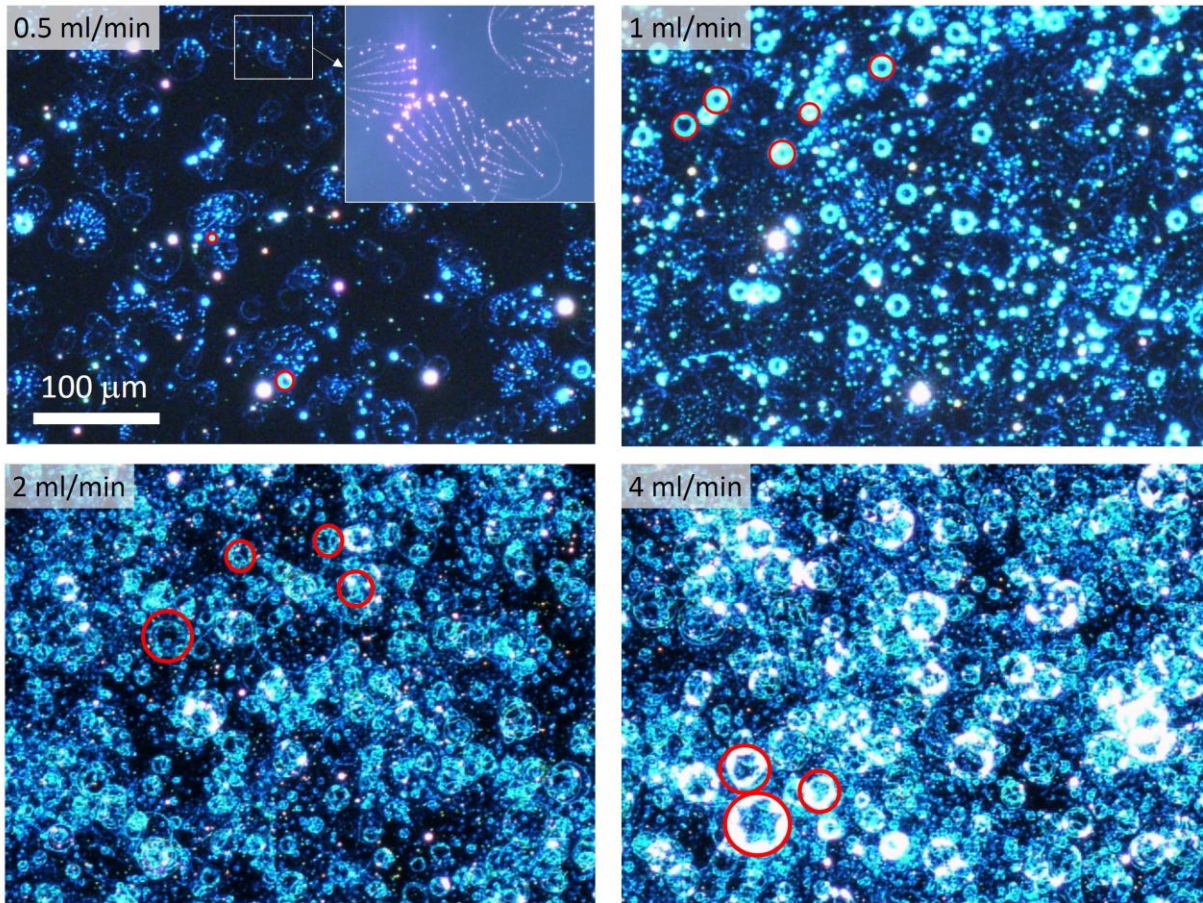
Figure S7. Optical microscopy images showing the effect of precursor solution feed rate during spraying on film deposition. The dark field optical microscopy images of dried droplets in (a), obtained with liquid feed rate of 0.5 ml min^{-1}, yields ~100 droplet s^{-1} cm^{-2}. Inset: Higher resolution image of a few droplets. (b) 1 ml min^{-1} resulting in ~200 droplet s^{-1} cm^{-2}. (c) 2 ml min^{-1} resulting in ~400 droplet s^{-1} cm^{-2}, and (d) 4 ml min^{-1} resulting in ~800 droplet s^{-1} cm^{-2}.
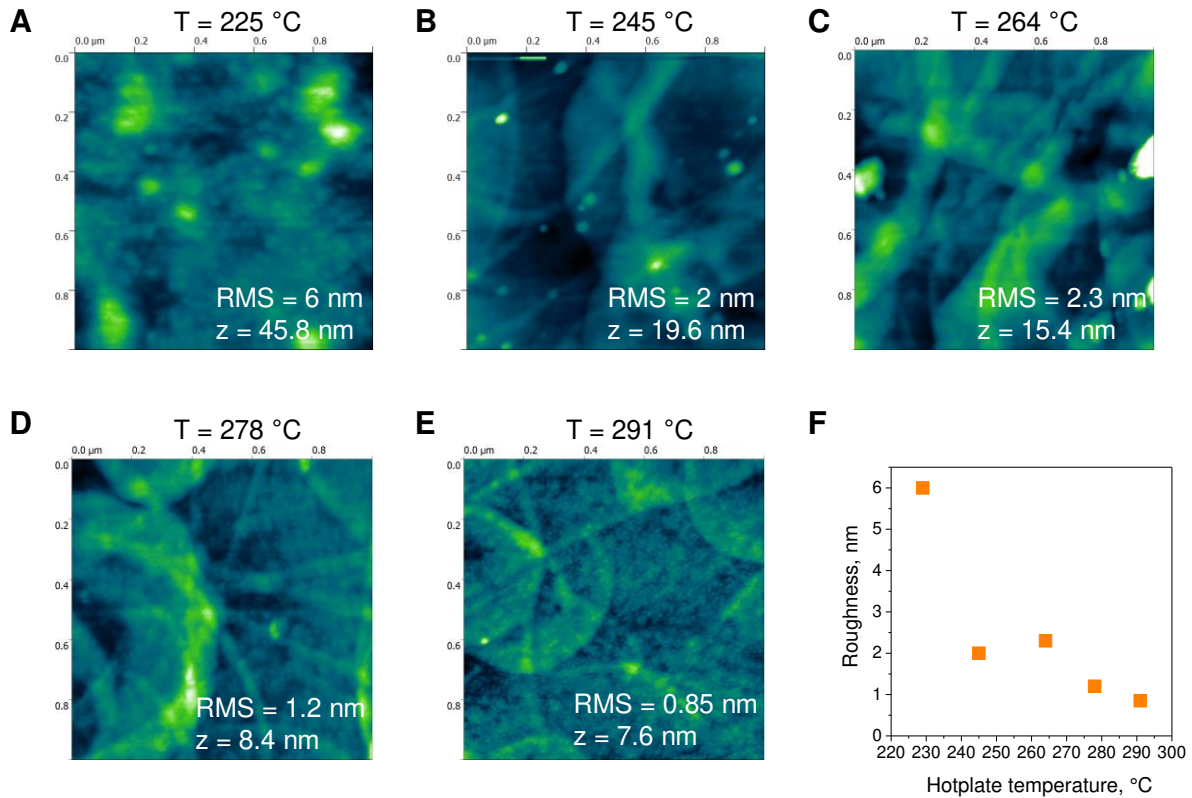
Figure S8. (a-e) AFM images of In_2O_3 layers deposited onto Si^{++}/SiO_2-100nm substrate at different temperatures; field of view 1×1 µm. (f) Surface roughness of the In_2O_3 layers as a function of hotplate temperature. The z value in each panel indicates the maximum height feature represented by the lighter colour shade regions.

Section S4. High Resolution Transmission Electron Microscopy (HRTEM)

The morphology, structure and crystallography of In_2O_3 layers grown by ultrasonic spray pyrolysis at 250ºC and 220ºC, and by spin-coating on Si^{++}/SiO_2 substrates followed by thermal annealing at 250ºC, were investigated by High Resolution Transmission Electron Microscopy (HRTEM). The obtained HRTEM images and FFT diffractograms obtained are all consistent with a cubic In_2O_3 lattice with the $Ia\bar{3}$ symmetry and a lattice parameter of $a = 10.10$ Å, in line with the GID measurements in **Figure 6**. **Figure S9a** shown an HRTEM image of three elongated single crystals within an In_2O_3 layer sprayed at 250ºC in edge-on position. **Figure S9b** is the corresponding FFT diffractogram of the central crystal, which is oriented exactly parallel to the [110] zone axis of the In_2O_3 lattice, while the two adjacent crystals on either side are slightly tilted and twisted about the [001] growth axis by less than 5º. Since this is a common

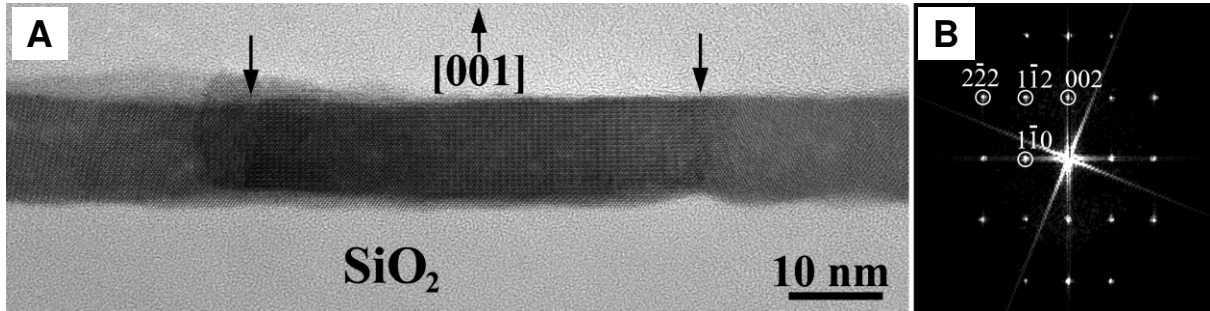trend among the majority of crystals comprised in this film, a prevalent (001) growth mode can be considered.

Figure S9. (a) Cross-section HRTEM image of part of an In_2O_3 thin film sprayed at 250°C on SiO_2, where three successive single crystals and their atomic structure are shown. Projected interfaces between crystals are depicted by arrows. (b) Corresponding FFT diffractogram of the central crystal showing its perfect alignment along the [110] projection direction, whereas neighboring crystals are oriented slightly off the specific axis.

On the contrary, In_2O_3 layers spayed at 220°C (below Leidenfrost temperature) are nanocrystalline as can clearly be seen in the dark-field (DF) TEM micrograph of **Figure S10a**. Nanocrystals of 3-6 nm in diameter do not share any common growth direction and are randomly oriented (**Figure S10b**). A similar nanocrystalline structure is also observed for spin-coated In_2O_3 layers, with the only difference being its ultra-thin thickness ($\cong 3$ nm) as compared to the 100 nm-thick sprayed layers (deposited below Leidenfrost temperature).
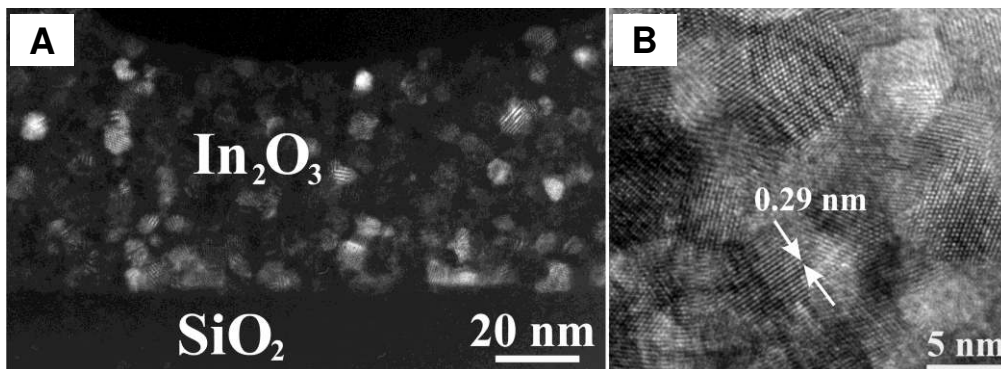

Figure S10. (a) DF TEM micrograph illustrating the random distribution of crystallites inside a spin-coated nanocrystalline In_2O_3 layers, grown at 220°C. (b) HRTEM of the nanocrystals showing their atomic structure. The {222} crystal planes are the most commonly observed planes in In_2O_3 nanocrystals (*d*-spacing = 0.29 nm).

SI References

[1]   L. H. J. Wachters and N. a. J. Westerling, *Chem. Eng. Sci.* **1966**, *21*, 1047.

[2]   Engineers Edge, "Convective Heat Transfer Coefficients Table Chart."
        http://www.engineersedge.com/heat_transfer/convective_heat_transfer_coefficients__1
        3378.htm. Access: November 2016.

[3]   U. P. Muecke, G. L. Messing, and L. J. Gauckler, *Thin Solid Films* **2009**, *517*, 1515.

[4]   C. Josserand and S. T. Thoroddsen, *Annu. Rev. Fluid Mech.* **2016**, *48*, 365.